American Mineralogist, Volume 90, pages 1506–1517, 2005

Raman spectroscopy and vibrational analyses of albite: From 25 °C through the melting temperature

DAVID A. MCKEOWN*

Vitreous State Laboratory, The Catholic University of America, 620 Michigan Avenue N.E., Washington, D.C. 20064, U.S.A.

ABSTRACT

Raman spectra were collected for crystalline albite from 25 °C to above the 1118 °C melting temperature, where vibrational assignments for the crystal spectra were determined by lattice dynamics (LD). The Raman spectra and associated vibrational assignments are reported for triclinic albite ($NaAlSi_3O_8$) at 25 °C and monoclinic albite at 1060 °C. The 25 °C calculations determined that localized T-O stretch and O-T-O bend modes are above 900 cm^{-1} (where T = Si,Al), while motions from the aluminosilicate tetrahedral cage mixed with Na displacements occur in modes as high as 814 cm^{-1}. Vibrational modes for the most prominent peaks in the spectrum, between 350 and 550 cm^{-1}, are dominated by four-membered tetrahedral ring deformations. For completeness, calculated infrared mode frequencies and their atomic displacements are reported for the 25 °C structure and compared with normal mode calculation results and observed infrared mode frequencies presented by von Stengel (1977). At higher temperatures, modes above 550 cm^{-1} broaden and shift to lower frequencies by 15 to 27 cm^{-1}; modes below 550 cm^{-1} broaden, but experience little, if any frequency shifts. Albite melted sluggishly, was completely liquid at 1320 °C, and remained amorphous upon cooling to room temperature. At frequencies above 550 cm^{-1}, the crystalline albite peaks, and possibly their vibrational assignments, can be correlated to Raman bands for albite glass. Spectral differences below 550 cm^{-1} between crystal and glass correspond to changes of average tetrahedral ring type upon melting, as shown by Taylor and Brown (1979).

INTRODUCTION

Raman spectroscopy has been used to characterize the structure of geologically interesting materials, such as feldspar-composition glasses (i.e., Matson et al. 1986; McKeown et al. 1984; McMillan et al. 1982). Structural characterization of these glasses can be used to predict certain physical properties (such as viscosity) of the corresponding melt (Mysen et al. 1980), so that the behavior of certain volcanic magmas can be better understood. Empirical vibrational assignments to the Raman spectral features of these glasses have been frequently determined from studies that compare spectra from chemically identical crystal-glass pairs (Brawer and White 1975; McKeown et al. 1984; McMillan et al. 1982). Using known crystal structures in these studies, comparisons between spectra of a crystal-glass pair can be used to make inferences about the glass structure. This study attempts to go one step further by using lattice dynamics (LD) calculations to determine vibrational assignments to the Raman spectral features of crystalline albite ($NaAlSi_3O_8$) and realistically map those assignments to similar features in the glass spectra, while drawing upon the results of earlier work on albite glass.

The purpose of this study is to determine how the Raman spectra and associated vibrational assignments of crystalline albite change upon heating from room temperature to above the melting temperature. The Raman spectrum and LD calculations are presented for the ordered albite structure at 25 °C. The calculations were repeated for albite at 500, 750, 980, and 1060 °C using the structural parameters reported in a high-temperature crystal-structure study (Winter et al. 1979) and the observed mode frequencies in the corresponding spectra at temperature.

Albite is an important rock-forming alkali feldspar mineral that consists of a tetrahedral cage structure that has cavities containing Na ions (Ribbe 1975; Smith 1974). The cage is comprised of linked four-membered tetrahedral rings, where Al atoms in the ordered structure occupy the $T_1(o)$ tetrahedral site that is bonded to four surrounding silicate tetrahedra through shared oxygen atoms (Fig. 1). Albite undergoes a triclinic to monoclinic phase transition near 980 °C, where the Al and Si randomize at the tetrahedral sites, so that each site is 25% occupied by Al and 75% occupied by Si (Winter et al. 1979). The cage structure around the Na sites also adjusts to a higher-symmetry configuration at temperatures above the phase transition.

Albite has been used to model the structure of feldspar composition glasses in X-ray studies (Taylor and Brown 1979; Taylor et al. 1980), as well as in Raman studies (McKeown et al. 1984). The Raman spectrum of albite has been presented in studies about silicate mineral characterization in terrestrial and extraterrestrial samples (White 1975; and Freeman et al. 2003). However, no vibrational assignments have been presented for the Raman spectral features of crystalline albite using an LD model based on the crystal structure. Comparison of the room-temperature Raman spectra of albite crystal and glass (McKeown et al.

* E-mail: davidm@vsl.cua.edu

0003-004X/05/0010–1506$05.00/DOI: 10.2138/am.2005.1726

1984) led to the conclusion that the local Si and Al environments in both materials are similar. Tetrahedral Al in albite glass was further verified by X-ray absorption spectroscopy (McKeown et al. 1985). X-ray diffraction and scattering studies of albite (Taylor and Brown 1979) indicated a long-range structural rearrangement upon melting, when the four-membered ring-based structure in crystalline albite converts to a stuffed tridymite-type six-membered ring structure in the melt; this structure persists in the glass at room temperature (Taylor et al. 1980).

In this study, the observed fundamental mode frequencies used for the calculations were obtained from the Raman data. With the development of high-throughput Raman systems (Goncharov and Struzhkin 2003), good signal-to-noise spectra are now routinely collected, even for weakly scattering materials like albite. Raman-active fundamental mode frequencies are associated with narrow peaks that are more accurately determined than frequencies associated with broader IR bands. Since room-temperature albite has triclinic symmetry (Fig. 1), there is one Raman-active vibrational species (A_g), so that one unpolarized spectrum is needed to determine all observed Raman-active fundamental mode frequencies (Fig. 2).

Normal mode calculations for the alkali feldspars albite, microcline ($KAlSi_3O_8$), and sanidine [$(K,Na)(AlSi)_4O_8$], were presented by von Stengel (1977). For albite, the infrared (IR) spectra, calculated Raman- and IR-mode frequencies, as well as force constant values determined from the normal mode calculations were reported. However, no vibrational assignments based on the albite calculations were presented. Similar to the approach used here, a valence force potential model was constructed, where the corresponding force constant values were varied so that calculated fundamental mode frequencies were best fit to observed mode frequencies determined from the spectra. In contrast to the approach used here, the observed frequencies were determined from the IR spectra, because at the time, a more complete set of fundamental mode frequencies was reliably determined from the IR spectra than from the Raman data. Since the present Raman study uses a different valence force potential model than that employed by the IR study (von Stengel 1977), the resulting force constant values, mode frequency fits, and eigenmodes will be compared with those reported by von Stengel (1977).

Experimental method

The albite sample used in this study was obtained from the Rutherford Mine in Amelia, Virginia (NMNH no. C5390-1). Phase identification of the sample was verified by powder X-ray diffraction. Earlier chemical analyses of the sample by Kracek et al. (1951) indicated close to end-member composition, where K_2O and CaO impurity concentrations were found to be 0.29 and 0.0 wt%, respectively; therefore, the ordered low albite structure is assumed (Ribbe 1975). Raman measurements were made using two colorless, clear albite cleavage fragments, which were approximately 800 μm in diameter by 40 μm thick. Scanning electron microscopy-energy dispersive spectroscopic (SEM-EDS) analyses of the samples before and after melting show little compositional variation.

Each albite fragment was placed in a small Pt crucible within a Linkam model TS1500 heating stage. Two heating experiments were performed to verify the spectral trends. Both experiments were done in air at room pressure, with a ceramic heat shield placed over the crucible within the ceramic heating block. The stage heated the sample to 500, 750, 980, 1060, 1100, 1200, 1245, 1270, and 1320 °C. The heating rate was 100 °C per minute up to 500 °C, 80 °C per minute up to 750 °C, 60 °C per minute up to 980 °C, 30 °C per minute up to 1060 °C, and 20 °C per minute for temperatures above 1100 °C. The stage was held at each temperature for at least one minute before any data were collected to insure thermal equilibrium of the sample. The sample was then cooled to 1075, 540, and 25 °C, using the same rates outlined above. Under identical conditions, the heating stage thermocouple was temperature calibrated by melting KNO_3 (T_f = 333 °C), Na_2SO_4 (T_f = 884 °C), and $NaSiO_3$ (T_f = 1088 °C). All albite temperatures were corrected with the resulting calibration curve, so that the reported temperatures are within ± 5 °C of actual.

Raman spectra were gathered using a single-grating spectrograph-notch filter system (Goncharov and Struzhkin 2003). An EXCEL Model 3000 Ar^+ laser provided 4579 Å wavelength incident light that was directed through a broad band polarization rotator (Newport Model PR-550) to the laser microscope that guided the laser light down to the sample surface through a long working-distance Mitutoyo 10× microscope objective. The laser light was focused to a 10 μm diameter spot on the {001} cleavage surface of the albite fragment. The laser light power was approximately 20 mW at the sample. Room-temperature unpolarized spectra were gathered with the sample in the heating stage, in back-scattering geometry with the heating stage silica window and analyzer polarizer out of the scattered light path. For the heating experiments, the laser light went through the silica glass window of the heating stage, and through a 1 mm diameter hole in the heat shield. Polarized spectra were gathered in the same geometry, where the scattered light was directed through an analyzer polarizer in the microscope column. The polarizer was set to one orientation for all polarized spectra collected. After the analyzer, the scattered light proceeded through holographic notch and super-notch filters (Kaiser Optical Systems), which reduced the Rayleigh scattered light intensity by ten optical densities. The notch filters were oriented in the scattered light path so that the filter cut-off frequency in the collected spectra was minimized to near 60 cm^{-1} from the laser line. Due to the many relatively narrow spectral features in the room temperature data, the incident slits of the spectrograph were set to 3 cm^{-1} resolution. Due to broadening of the spectral features at temperatures above 25 °C, the slits were widened to 4 cm^{-1} resolution to improve the signal-to-noise ratios of the data. The JY-Horiba HR460 spectrograph used a 1200 gr/mm grating (Richardson Grating Laboratory) that was set to disperse the Stokes scattered light from the sample on to a 2048 × 512 element Peltier cooled CCD detector (Model DU440BV supplied by Andor Technology). The spectrograph was frequency calibrated using a Ne lamp and CCl_4 so the recorded frequencies are accurate to within ±1 cm^{-1}. Parallel-polarized (VV) or cross-polarized (HV) spectra were gathered where the incident laser light was vertically or horizontally polarized, respectively, as it entered the laser microscope. Each spectrum is an average of 25 accumulations, collected for 10 s each.

Different sets of Raman spectra were gathered for each temperature range. From room temperature to 750 °C, one unpolarized Raman spectrum was collected at each temperature, because triclinic albite has only one Raman-active vibrational species (A_g). At 980 and 1060 °C, VV and HV-polarized spectra were collected, because monoclinic albite has two Raman-active vibrational species: A_g corresponds to the VV spectrum, and B_g corresponds to the HV spectrum. Unpolarized spectra were also gathered at 980 and 1060 °C for direct comparison with the unpolarized spectra gathered at lower temperatures. VV, HV, and unpolarized spectra were also gathered during the cooling part of the cycle of each run.

All spectra were corrected for notch filter, grating efficiency, and detector quantum efficiency effects on the scattered light intensities. Notch filter corrections were effective down to near 100 cm^{-1}; Raman intensities of features below 100 cm^{-1} in the spectra presented are probably distorted. The heating stage window in the incident and scattered light paths caused a –0.4 cm^{-1} frequency shift in the resulting spectra, which was corrected. Despite using the shortest wavelength laser light available at significant power levels from the Ar^+ laser, black-body radiation from the sample and the surrounding heating stage became significant, especially above 1000 °C; this caused a noticeable background that increased in intensity from low to high Raman shift. To correct for black-body effects from the heating stage, a blank heating experiment was performed under identical conditions, with no sample in the heating stage. A blank spectrum was subtracted from the albite + heating stage spectrum at each temperature, which eliminated most of the black-body contributions. Black-body contributions from the sample itself are evident in the spectra at temperatures above 1200 °C.

Normal coordinate analysis

Triclinic ($C\bar{1}$) albite structure

A sixty-three atom cluster was used to simulate the triclinic albite structure at 25, 500, and 750 °C for the LD calculations at zero wavevector (Dowty 1987a). The space group symmetry, unit-cell parameters, and atom coordinates used for the LD model

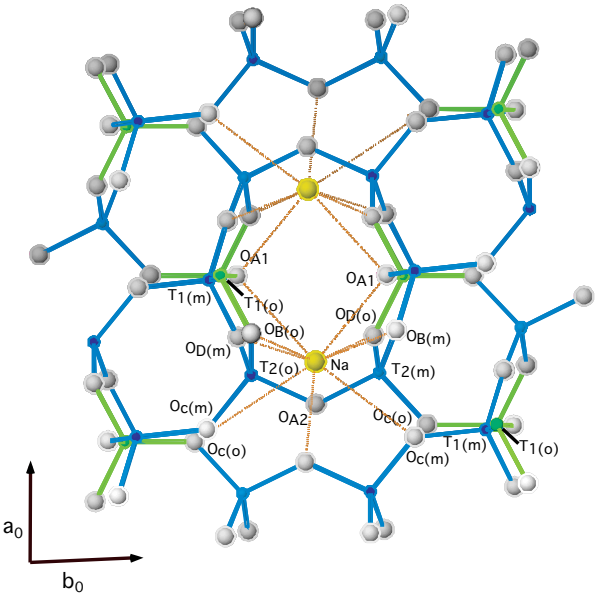

FIGURE 1. The **c** projection of the ordered triclinic albite structure at room temperature; representative atom types are indicated. Thick lines are Si-O (blue) and Al-O (green) bonds; thin orange lines are Na-O bonds.

are from Winter et al. (1979). The potential energy model used to describe the bonding within the structure model is based on a valence force potential (Kim et al. 1993) consisting of Si-O, Al-O, and Na-O bond stretching as well as O-Si-O, O-Al-O, and O-Na-O bond-bending interactions. The Na environment in albite includes a range of nine different Na-O distances, so two Na-O stretch force constants were used: Na-O(short) for distances less than 3.0 Å and Na-O(long) for distances greater than 3.0 Å. A total of 78 fundamental optical modes are predicted for the triclinic structure by factor group analysis (FGA), where 39 A_g modes are Raman-active, and 39 A_u modes are IR active, including three acoustic modes (Fateley et al. 1972; von Stengel 1977). Most room-temperature observed fundamental mode frequencies could be determined from the unpolarized spectrum that provided frequency targets for the calculations (Fig. 2). The calculations, in turn, provided guidelines for making a few additional fundamental mode selections, especially for some of the weaker spectral features. The theory predicts one fundamental Raman-active mode for the weak doublet peak near 1000 cm^{-1} and two fundamental Raman-active modes for the triplet peak near 400 cm^{-1}. Two weak peaks in the data at 414 and 1010 cm^{-1} are not described by the calculations, and are probably second-order overtones of the relatively large-amplitude fundamental modes at 207 and 505 cm^{-1}.

The LD calculations for the triclinic structure used a total of 190 interactions described by seven force constants (Table 1) that adequately depict the bonding environments in the structure, so that all calculated fundamental optical modes have non-zero frequencies. Initial calculations were performed for albite using force constant values for Si-O, Al-O, and Na-O stretching and O-Si-O, O-Al-O, and O-Na-O bending similar to those determined for equivalent environments in cyclosilicate and phyllosilicate structures (McKeown et al. 1993, 1999a, b). The seven force constants were varied to provide the best fit between the calculated and observed frequencies in the Raman spectrum (Fig. 2) and are similar to those determined for other silicate structures (McKeown et al. 1993, 1999a, b; Dowty 1987b). The fitting was accomplished by minimizing the root-mean-square (rms) deviation between the calculated and observed Raman-active fundamental mode frequencies (Dowty 1987a) (Table 2a); a final rms

TABLE 1. Force constant values determined for triclinic albite

Interaction	25 °C	500 °C	750 °C
Bond stretch			
Si-O	4.83 x 10^5 dyne/cm	4.76	4.69
Al-O	3.19	3.21	3.23
T-O	4.42	4.37	4.33
Na-O (short)	1.02	1.10	1.05
Na-O (long)	0.25	0.25	0.26
Bond bend			
O-Si-O	0.59 x 10^{-11} erg	0.59	0.59
O-Al-O	0.35	0.35	0.35
O-T-O	0.53	0.53	0.53
O-Na-O	0.06	0.06	0.06
Final rms (cm^{-1})	5.7	6.8	8.1

Note: T-O stretch and O-T-O bend values are listed for comparisons with Table 4 and are determined from: $k_{T\text{-}O} = 0.25k_{Al\text{-}O} + 0.75k_{Si\text{-}O}$ and $k_{O\text{-}T\text{-}O} = 0.25k_{O\text{-}Al\text{-}O} + 0.75k_{O\text{-}Si\text{-}O}$, respectively.

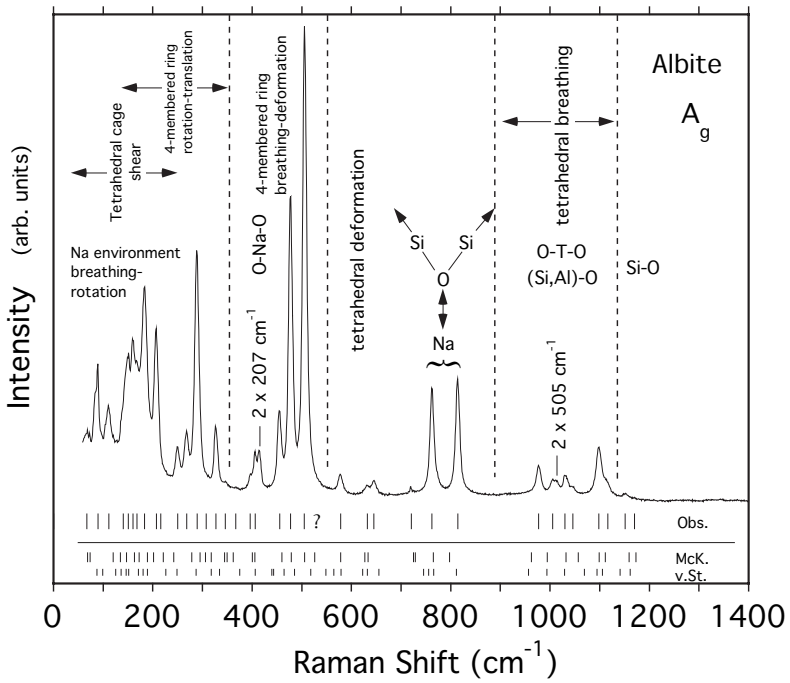

FIGURE 2. The unpolarized room-temperature Raman spectrum of albite. General vibrational assignments from the LD calculations are indicated. Observed fundamental mode frequencies are indicated and labeled as "Obs." Calculated mode frequencies are labeled: "McK." from this study and "v.St." from von Stengel (1977).

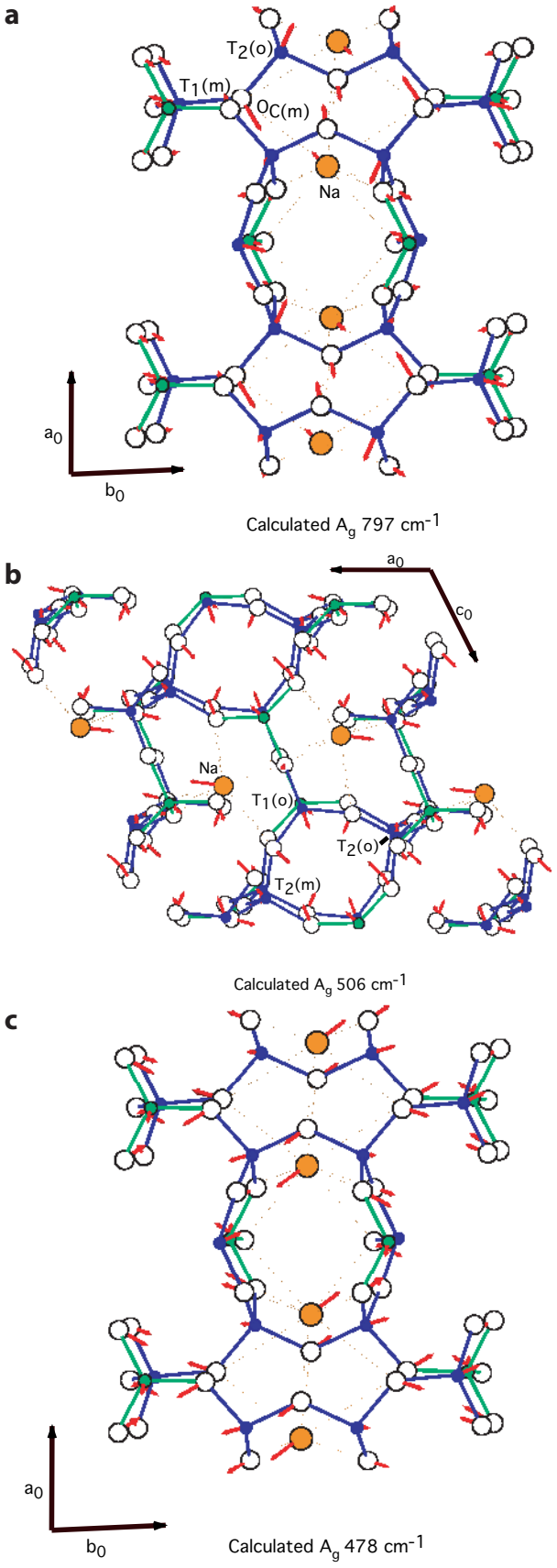

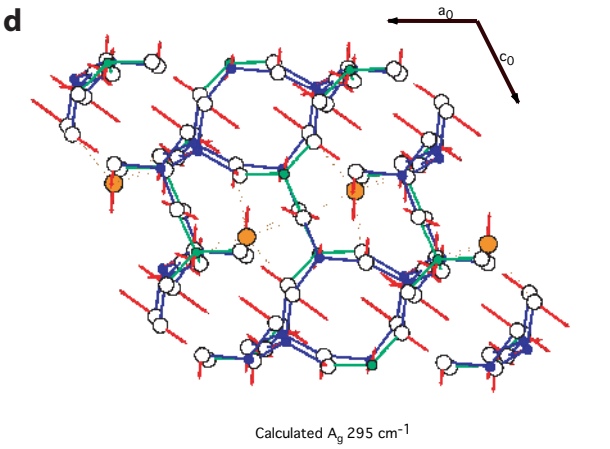

FIGURE 3. Eigenmode plots for four of the more prominent peaks in the Raman spectrum of albite. Atom types involved in some of the atomic displacements are labeled; see Figure 1 for the complete atom labeling convention. Calculated eigenmode frequencies are indicated. Thick lines are Si-O (blue) and Al-O (green) bonds; thin lines are Na-O bonds. Atom displacements are indicated by red arrows.

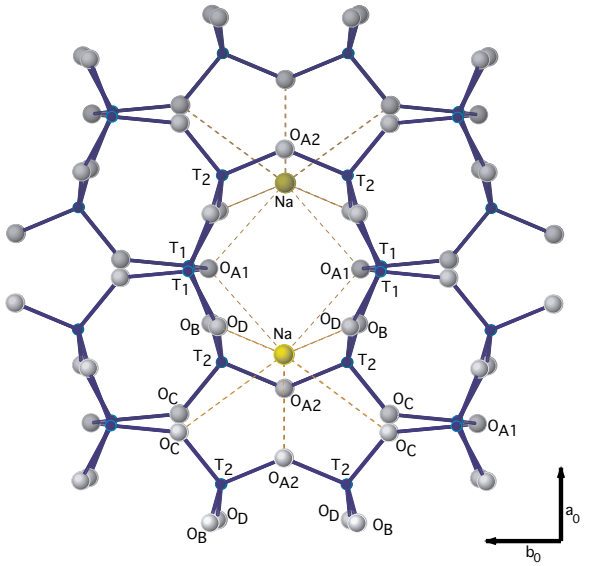

FIGURE 4. **c** axis projection of the monoclinic albite structure at 1060 °C; atom types are indicated. Thick lines are T-O bonds, where T = Si,Al; thin lines are Na-O bonds.

deviation of 5.7 cm^{-1} was obtained. The calculated frequency and the associated eigenmode for each Raman-active fundamental A_g mode are listed in Table 2a and plotted in Figure 2. Representative A_g eigenmodes calculated for prominent intensity modes are depicted in Figures 3a through 3d. For completeness, calculated IR-active modes from this study and observed IR mode frequencies from von Stengel (1977) are listed in Table 2b.

Monoclinic (*C*2/*m*) albite structure

A 62 atom cluster was used to simulate the monoclinic structures at 980 and 1060 °C (Fig. 4) for the LD calculations at zero wavevector. The potential energy model used to describe the bonding within these two structures is based on a valence force

TABLE 2A. Lattice dynamics fitting results of albite at 25 °C for the Raman-active A_g species: observed frequencies, calculated frequencies, and eigenmodes

ν_{obs}	ν_{calc}	A_g eigenmode description
1170 cm^{-1}	1173 cm^{-1}	Si-O stretch: T_2(m)-O_B(m), T_1(m)-O_D(m), T_1(m)-O_B(m),T_2(o)-O_D(m).
1151	1159	Si-O stretch: T_1(m)-O_D(m), T_1(m)-O_C(m), T_2(m)-O_B(m).
1116	1111	T_1(o) tetrahedral base breathing and T_1(o)-O_{A1} stretch.
1098	1099	Si tetrahedra deformation: Si-O stretch, tetrahedral base breathing.
1046	1056	Si-O stretch: T_2(m)-O_D(o); Al-O stretch: T_1(o)-O_D(o), T_1(o)-O_c(o).
1030	1032	Si-O stretch: T_1(m)-O_{A1}, T_2(o)-O_B(o); O-Al-O bend: O_{A1}-T_1(o)-O_B(o).
1005	994	Al tetrahedron deformation: T_1(o)-O_B(o) stretch, Si-tetrahedral base breathing.
977	962	O-Al-O bend: O_D(o)-T_1(o)-O_C(o); Si tetrahedral breathing / deformation.
814	797	Si-O-Si bend: T_1(m)-O_C(m)-T_2(o); Na ±**ab** (Na-O_C(m) stretch).
762	764	Tetrahedral deformation: T_2(o)-O_{A2}-T_2(m) bend; Na-O_{A2} stretch.
720	728	O-Al-O bend: O_D(o)-T_1(o)-O_C(o); Si, Al-tetrahedral deformation; Na-$O_{A1,}$ Na-O_B(o) stretch.
720	725	T_1(o)-O_C(o) stretch; Na, Al, O ±**b** motion; Si, Al-tetrahedral deformation; Na-O_C(o) stretch.
645	633	Al-O-Si bend: T_1(o)-O_B(o)-T_2(o); Na-O_{A1} stretch; (Si, Al) tetrahedra deformations; O-Na-O bend.
632	627	T_2(m) tetrahedral breathing: T_2(m)-O_B(m) stretch; (Si, Al) tetrahedral deformation; Al ±**c**; Na-O_{A1} & Na-O_B(o) stretch: O-Na-O bend.
578	578	*ac*-plane translations: Si, Al-tetrahedral deformations; Na coordination deformation: O-Na-O bend.
528*	526	(Si, Al) tetrahedral deformations; Na-O_C(m) & Na-O_{A1} stretch.
505	506	Compression of four-membered tetrahedral rings along **c**; Na-coordination expansion: Na ±**a**; O_{A1}-Na-O_{A1} breathing.
477	478	Tetrahedral ring compression in **ab**-plane; Na-coordination expansion: Na ±**ab**: Na-O_C(o) stretch.
455	460	Na-coordination deformation: Na ±**c**: O_B(m)-Na-O_{A2} bend; Al-tetrahedral rotation around Al-O_C(o).
406	405	Deformation of Al-tetrahedra || **c**; Ring deformation: bridging oxygen to center, T away from ring center.
396	400	**b**-axis projection: four-membered ring deformation: bridging O atoms: O_C(m) & O_D(m) toward ring center, tetrahedral sites away from ring center except for Al.
367	362	O_B(m)-T_2(m)-O_{A2} bend; four-membered ring breathing-rotation || **a**.
346	349	Si-tetrahedra shearing || **b**; Al-tetrahedra shearing || **c**; O-Na-O bends.
346	344	Tetrahedral compression || **b**; O_A(2) ± **c**; Si-O-Al compression.
327	317	Tetrahedral ring shear/rotation || **b**; Na ± **b**, Na environment compression || **b**.
307	306	Tetrahedral cage compression-expansion || **b**; Na ± **b**, Na environment extension || **bc**.
289	295	Tetrahedral cage shear within **ac** plane; Na ± **a**.
268	278	Tetrahedral cage rotation-breathing || **b**, shear in **bc** plane; Na ± **c**.
250	242	Tetrahedral ring translation along **b**; tetrahedral cage compression || **b**; Na ± **a**, Na environment deformation ± **b**.
216	221	Tetrahedral cage shear-rotation around **c**, expansion-contraction perp. **b**; Na ± **a**.
207	201	Tetrahedral ring shear || **a**; Na ± **a**, Na environment expansion || **b**; tetrahedral cage expansion-contraction || **b**.
183	189	Na-tetrahedral structural unit rotation-shear || **c**; Na ± **b**.
168	172	Na-tetrahedral cage rotation-shear || **c**.
160	162	Overall shear || **c**; tetrahedral ring compression-shear || **c**.
150	147	Overall compression-expansion || **b**; Na ± **b**; tetrahedral cage rotation || **b**.
140	135	Tetrahedral cage shear || **b**.
111	120	Overall structural compression-expansion in **bc**-plane.
89	73	Tetrahedral cage shear along **a**.
67	69	Tetrahedral ring shear || a; looking down c: tetrahedral cage compression || **b**.

Note: more dominant atomic displacements are listed first.
*From White (1975) and not used in the fitting.

potential consisting of T-O and Na-O bond-stretching as well as O-T-O and O-Na-O bond-bending interactions (where T = Al,Si). Since each disordered T-site contains 75% Si and 25% Al atoms in these structures, a similarly weighted atomic mass was used for each tetrahedral site. The Na environment for this structure also includes a range of Na-O distances, so that Na-O(short) and Na-O(long) stretch constants were set up similarly to those used for the triclinic structure.

A total of 78 fundamental optical modes are predicted for the monoclinic albite structure by FGA. Twenty A_g and 19 B_g modes are Raman-active and 18 A_u and 21 B_u modes are IR active, including three acoustic modes (Table 3). Many of the fundamental mode frequencies could be determined from the A_g and B_g spectra that provided frequency targets for the calculations. Since most of the peaks in these Raman spectra are broad, several calculated modes could be assigned to each peak, where frequency ranges under broad peak envelopes were targets for the calculated mode frequencies.

TABLE 3. Irreducible representations for the monoclinic albite structure at 980 and 1060 °C

Atom types	Site symmetry	A_g (R)	B_g (R)	A_u (IR)	B_u (IR)
Na, O_{A2}	m	2	1	1	2
O_{A1}	2	1	2	1	2
T_1, T_2, O_B, O_C, O_D	1	3	3	3	3
N_{total}		20	19	18	21

Note: R and IR indicate Raman-active and infrared-active, respectively. A_u and B_u species include 1 and 2 acoustic modes, respectively.

The LD calculations for the monoclinic structures each used a total of 190 interactions described by five force constants (Table 4) that adequately depict the bonding environments in each structure. Initial calculations were performed for the monoclinic 980 °C structure using force constant values determined for the triclinic 550 °C structure. Initial force constants involving the tetrahedral sites were weighted sums of the final Si and Al force constants determined for the 550 °C structure (i.e., $k_{T\text{-}O} = 0.25k_{Al\text{-}O} + 0.75k_{Si\text{-}O}$). The five force constants were varied to give the best fit between calculated and observed frequencies. The O-Na-O bending force constant was varied to zero and was subsequently constrained to zero (Table 4). The calculated frequency and the

TABLE 4. Force constant values determined for monoclinic albite

Interaction	980 °C	1060 °C
Bond stretch		
T-O	4.21 × 10^5 dyne/cm	4.22
Na-O (short)	1.01	1.01
Na-O (long)	0.17	0.16
Bond bend		
O-T-O	0.52 x 10^{-11} erg	0.53
O-Na-O	0	0
Final rms	10.5 cm^{-1}	10.0

TABLE 2B. Lattice dynamics results of albite at 25 °C for the IR-active A_u species: observed frequencies, calculated frequencies, and eigenmodes

ν_{obs}*	ν_{calc}	A_u eigenmode description
1160 cm^{-1}	1175 cm^{-1}	Si-O Stretch: T_2(m)-O_B(m), T_2(o)-O_c(m); O-Si-O breathing: O_D(m)-T_1(m)-O_C(m).
1142	1145	Si-O Stretch: T_1(m)-O_D(m), T_1(m)-O_C(m); O_{A2}-T_2(o)-O_B(o) bend.
1106	1120	T_1(m) tetrahedral base breathing; T_1(m)-O_{A1}, T_1(o)-O_D(o), T_2(o)-O_c(m) stretch.
1096	1098	Si-O stretch: T_2(m)-O_{A2}, T_2(o)-O_{A2}; O-T-O breathing: O_B(o)-T_1(o)-O_D(o), O_D(m)-T_1(m)-O_B(m).
1048	1054	T_1(m) tetrahedral base breathing; Si-O stretch: T_1(m)-O_D(m), T_2(m)-O_D(o), T_2(o)-O_B(o); Al-O stretch: T_1(o)-O_D(o).
1032	1036	T_1(m) tetrahedra breathing; T-O stretch: T_1(m)-O_{A1}, T_2(m)-O_{A2}, T_1(o)-O_{A1}, T_2(o)-O_{A2}.
1004	1007	T_1(m)-O_{A1}, T_2(m)-O_B(o) stretch; O_B(o)-T_1(o)-O_{A1} deformation; O_D(o)-T_2(m)-O_{A2} breathing.
988	969	T_1(m) tetrahedral base breathing; T_1(m)-O_C(m), T_2(m)-O_C(o), T_2(o)-O_{A2} T_1(o)-O_C(o) stretch; Al tetrahedra deformation.
786	792	Si-O-Si deformation: T_2(m)-O_{A2}-T_2(o), associated with Na-O_{A2} stretch, Na ±**a**. T_1(o)- and T_1(m)-tetrahedral deformations.
760	749	Si-O-Si deformation: T_1(m)-O_C(m)-T_2(o), associated with Na-O_C(m) stretch, Na ±**b**; T_1(o)-O_B(o) and T_2(m)-O_{A2} stretch.
742	725	T_1(o),T_2(m)-tetrahedral deformation; T_1(m)-O_B(m), T_2(o)-O_{A2} stretch; Na-O_C(m) stretch.
722	713	Tetrahedral deformation; T_1(o)-O_C(o) stretch; Na ±**b**.
648	643	Tetrahedra deformations along **a**; O_D(m)-Na-O_D(o) breathing.
607	628	(Si, Al) tetrahedral deformation; T_1(m)-O_{A1}-T_1(o) deformation || **a**; Na±**ab**.
589	570	Si-tetrahedral breathing; Na ±**b**, against surrounding tetrahedral cage.
530	556	Tetrahedral ring compression-expansion || **b**; Na ±**ab**: against tetrahedral cage motion ±**b**.
474	502	T_1(o) tetrahedral rotation || **a**; T_1(m) tetrahedral rotation || **b**; T_2(o)-, T_2(m)-tetrahedral deformation; Na±**a**: O_{A1}-Na-O_{A1} bend-shear || **a**.
462	470	Na±**b**; tetrahedral ring translation along **b**, expansion-compression || **b**; O_{A1} ±**a**.
426	439	Na± **c**: O_{A1} ± **b**; tetrahedral ring breathing-deformation: T into ring center, bridging-oxygen away from ring center.
400	412	T_1(m)-, T_1(o)-tetrahedra rotation-shear around **c**, four-membered tetrahedral ring compression-expansion; O_{A1} ± **a**; O_{A2} ± **a**.
387	381	O_{A2} ± **a**; tetrahedral cage shear: compression-expansion || **b**; Na± **c**.
375	360	Tetrahedral four-membered ring compression-expansion || **ac**-plane.
–	353	Tetrahedral four-membered ring compression-expansion || **c**. O_B(o)± **ac**; O_C(m)± **c**.
336	341	Structural shear || **b**, compression-expansion along **b**.
–	315	Tetrahedral cage shear along **b**, rotation || **a**; Na ± **a**.
–	307	O_{A2} ± **c**. structural shear within **bc**-plane.
–	296	Tetrahedra rotation around **c**; Na ± **ab**.
276	280	Structural shear along **b**.
–	267	Structural shear along **b**.
252	245	Tetrahedral cage shear-rotation around **b**; tetrahedral cage compression-expansion || **b**; Na ± **b**.
217	215	Tetrahedral cage shear-rotation || **c**; Na ± **c**.
200	202	O_B(o) ± **b**; cage shear (rotation || to) along **b**; Na ± **a**.
186	193	O_{A1} ± **b**; tetrahedral four-membered ring expansion-compression within **ac** plane; Na ± **b**.
165	187	O_D(m)± **c**; Overall shear-rotation around **c**.
146	166	O_{A2} ± **c**; tetrahedral cage compression-expansion || **b**.
92	86	Tetrahedral cage compression-expansion within **ac** plane.

Note: Three acoustic modes are not listed. More dominant atomic displacements for each eigenmode are listed first.
* From von Stengel (1977) and not used in the fitting procedure.

associated eigenmode for each fundamental A_g and B_g mode at 1060 °C are listed in Tables 5a and 5b, respectively.

RESULTS AND DISCUSSION

Room temperature albite

Raman spectrum—calculated A_g modes. The measured unpolarized albite spectrum (Fig. 2) is similar to those presented by Rossman (2004), McKeown et al. (1984), and White (1975), but has improved signal-to-noise levels and resolution, so that more weak modes are visible. Frequencies of the six most prominent peaks are very close to those listed for highly ordered low albite (Freeman et al. 2003). Several spectra were collected from various albite fragments at different crystallographic orientations with respect to the incident laser light polarization. The majority of the spectral features do not change significantly. Peaks at 1116, 1098, and 160 cm^{-1} can have larger relative amplitudes, while peaks at 814, 762, and 455 cm^{-1} can have smaller relative amplitudes than those shown in Figure 2. Two partially resolved peaks or shoulders can also be seen in some spectra near 770 and 307 cm^{-1} (not observed in Fig. 2). The 770 cm^{-1} feature was not fit well by the LD model and may be associated with an additive mode of the prominent 477 and 289 cm^{-1} peaks.

The spectrum can be divided into four frequency regions based on the basic types of eigenmodes generated by the calculations (Fig. 2 and Table 2a). Calculated A_g mode frequencies from this study as well as from von Stengel's model are plotted in Figure 2 for comparison.

The weak peaks above 900 cm^{-1} are assigned to internal tetrahedral vibrations. The highest frequency peak at 1150 cm^{-1} has a shoulder near 1170 cm^{-1}, which is another fundamental mode according to the calculations. Both modes are dominated by Si-O stretch, where little, if any, Al motion is present. Below 1150 cm^{-1}, the modes are mixtures of Si-O and Al-O stretch as well as O-Si-O and O-Al-O bend motions.

Between 550 and 900 cm^{-1}, modes are less localized, and all atom types in the crystal structure are in motion. The highest-frequency modes where Na displacements take place are the peaks at 814 and 762 cm^{-1}, where Si-O-Si breathing motions as well as neighboring Na-O stretches dominate (Figs. 2 and 3a, and Table 2a). According to the calculations, the peaks at 720, 762, and 814 cm^{-1} correspond to four fundamental modes, where the best fit model assigns two modes to the weak 720 cm^{-1} peak. Modes near 600 cm^{-1} are dominated by tetrahedral breathing as well as Na-O stretch motions.

The most prominent peaks in the data are between 350 and 550 cm^{-1}, where the assigned vibrational modes are dominated by four-membered tetrahedral ring deformations. Modes within this frequency interval are clustered within two ranges: one from 450 to 550 cm^{-1}, and the other from 380 and 450 cm^{-1} (Fig. 2). The calculations place four fundamental modes between 450 and 550 cm^{-1}, where only three modes are clearly visible in the spectrum. The prominent 505 cm^{-1} peak has a high frequency shoulder, where the calculations place a fundamental mode at

TABLE 5A. Lattice dynamics fitting results of monoclinic albite at 1060 °C for the Raman-active A_g species: observed frequencies, calculated frequencies, and eigenmodes

ν_{obs}	ν_{calc}	A_g eigenmode description
?	1095 cm^{-1}	T-O Stretch: T_1-O_B, T_2-O_B.
1078	1073	T-O Stretch: T_1-O_C, T_2-O_D.
954	969	Tetrahedral base breathing; T_1-O_{A1}, T_2-O_{A2} stretch.
800	760	O_{A1}-T_1-O_D and O_{A2}-T_2-O_C bend; T_2-O_C-T_1 bend; Na ± a; Na-O_D stretch; O_D-Na-O_D bend.
745	734	T_1-O_B stretch; T_1-O_B-T_2bend; Na-O_B stretch; Na ± **c**; O_B-Na-O_B bend.
?	720	T_1-O_{A1}-T_1, T_2-O_{A2}-T_2bend; Na ± **ac**; Na-O_{A2} stretch; O_{A1}-Na-O_{A1} bend.
632	636	Tetrahedral base breathing; T_2-O_{A2} ± **a**; Na ± **a**; Na-O_{A2} stretch; O_{A1}-Na-O_{A1} breathing.
?	529	four-membered ring contraction || **c**; Na ± **b**.
505	516	Na ± **b**; O_B-Na-O_B bend; four-membered tetrahedral ring expansion || **ac**.
468	455	Na ± **a**; tetrahedral cage expansion-contraction || **b**; looking down **b**: bridging oxygen breathing in four-membered rings.
406	413	four-membered ring deformation: bridging O atoms toward ring center, T away from ring center; O_{A1} ± **b**, O_{A2} ± **a**.
?	360	Tetrahedral cage: T toward cage center, bridging O atoms away from cage center; Na ± **a**.
330	319	four-membered ring rotation || **b**; O_{A2} ± **b**; Na environment shear || **b**.
288	287	O_C ± **b**; four-membered ring rotation || **b**, structural shear in **ab** plane.
251	242	four-membered ring & Na environment shear in **ab** plane; Na ± **c**.
197	192	Tetrahedra cage shear in plane bisecting **ac**; Na ± **a**; O_{A1} ± **b**.
166	175	Tetrahedra cage shear within **bc** plane: rotation || **b**; Na ± **ac**.
110	123	four-membered ring shear-rotation || **b**; compression along **b**; Na ± **ab**; O_{A2} ± **b**.
92	101	Na environment & tetrahedra cage shear in **bc** plane: motions ± **c** ; O_{A1} ± **b**.
69	49	Tetrahedra cage rotation || **b**; shear within **ab** plane; Na ± **c**, O_{A1} ± **b**.

Note: More dominant atomic displacements for each eigenmode are listed first.

TABLE 5B. Lattice dynamics fitting results of albite at 1060 °C for the Raman-active B_g species: observed frequencies, calculated frequencies, and eigenmodes

ν_{obs}	ν_{calc}	B_g eigenmode description
?	1087 cm^{-1}	T-O stretch || **a**: T_1-O_{A1}, T_2-O_B.
1084	1076	T-O stretch: T_1-O_D, T_2-O_D; O_B-T_1-O_{A1} and O_{A2}-T_2-O_C bend.
?	1073	T-O stretch: T_1-O_C, T_2-O_D; T_1-tetrahedral base breathing; O-T_2-O bend.
1008	1020	Tetrahedral deformation: O_C-T_1-O_{A1} and O_{A2}-T_2-O_B bend; O_{A2} ± **b**.
954	965	T_1, T_2-tetrahedral base breathing; O_{A1} ± **c**; O_{A2} ± **b**.
723	748	O-T-O bend; Na ± **b**; O_D-Na-O_C bend.
632	634	Tetrahedral deformation; O_D-Na-O_B bend; O_{A1}-Na-O_B breathing; Na ± **c**.
?	560	Tetrahedral base breathing-rotation, T_1-O_D ± **ac**; Na ± **b**; O_{A2} stationary.
?	482	**c**-axis projection: T_2-tetrahedral breathing; T_1-tetrahedra ± **a**; O_{A2} ± **b**; Na ± **c**.
406	397	**c**-axis projection: tetrahedral cage: T to cage center bridging oxygen away from cage center; O_{A1} ± **a**; O_B-Na-O_D bend.
?	382	T_1-tetrahedral deformation: T_1-O_C ± **c**; other bridging O atoms - **c**; Na ± **b**; **a**-axis projection: four-membered tetrahedral rings: T to ring center, bridging O atoms away from ring center.
330	327	Structural shear || **a** in **ac**-plane; Na ± **c**.
288	308	Tetrahedral cage shear-deformation in **ac**-plane.
251	264	four-membered tetrahedral ring rotation || **a**; Na ± **c**; O_{A2} ± **b**.
?	211	Tetrahedral cage compression-expansion || **b**.
?	184	Tetrahedral cage compression-expansion || **b**; Na ± **b**.
158	159	Na ± **c**; O_{A2} ± **b**; four-membered tetrahedral ring: rotation || **a**, shear along **c**.
?	126	Tetrahedral cage rotation || **a** around Na cavity.
69	62	Tetrahedral cage rotation around Na; shear within **ab** plane.

Note: More dominant atomic displacements for each eigenmode are listed first.

526 cm^{-1}. Such a fundamental mode can be present in the data, but defining a specific observed frequency for this mode was not possible; however, White (1975) listed a 528 cm^{-1} mode for albite. The prominent 505 cm^{-1} peak is fit by the calculated 506 cm^{-1} mode, where the motions are dominated by four-membered tetrahedral ring compression-expansion as well as Na translation along **a** (Fig. 3b). The second strongest intensity peak at 477 cm^{-1} is fit by the calculated 478 cm^{-1} mode, where motions include Na-coordination expansion and tetrahedral ring compression within the **ab** plane (Fig. 3c).

Below 350 cm^{-1}, the lowest frequency modes include shear and deformation motions of larger atom clusters. Between 230 and 350 cm^{-1}, the eigenmodes are dominated by four-membered ring translation-rotation motions. Modes below 230 cm^{-1} are dominated by tetrahedral cage shear displacements in conjunction with Na environment breathing-rotation motions. The prominent 289 cm^{-1} peak (Fig. 2) is assigned to Na displacements perpendicular to **a**, as well as tetrahedral cage shear deformations along the **ac** direction (Fig. 3d).

IR spectra—calculated A_u modes. Calculated IR fundamental mode frequencies and their atomic displacements are reported in Table 2b, and can be compared with the measured IR spectra and calculated IR fundamental mode frequencies listed by von Stengel (1977). More recent IR studies of albite show similar spectra (Couty and Velde 1986; Atkinson et al. 1999). Calculated mode frequencies, determined from both models, reasonably match observed fundamental mode frequencies above 640 cm^{-1}. Below 640 cm^{-1}, calculated IR modes from each study have varying degrees of success fitting the observed mode frequencies. IR bands between 630 and 470 cm^{-1} are the most poorly fit by the model used here, where deviations between observed and calculated IR modes are as high as 28 cm^{-1} (Table 2b). This study calculated three IR modes at 315, 307, and 296 cm^{-1}, while von Stengel (1977) did not place anything within this frequency range. This range spans the spectral cut-off between the far- and mid-IR spectra reported by von Stengel (1977), where observed fundamental mode assignments were probably avoided. The three modes calculated by this study may correspond to weak modes

within the low-frequency shoulder of the 336 cm^{-1} band. Von Stengel (1977) also divided the IR spectra of the alkali feldspars into frequency ranges that are based on eigenmode type. The calculated IR modes for albite from this study are also grouped into four frequency ranges depending on the basic eigenmode type, different from those summarized by von Stengel (1977).

Eight modes are fit to the highest frequency bands between 980 and 1120 cm^{-1}. Six bands are observed (von Stengel 1977; Atkinson et al. 1999) where the additional calculated modes can be assigned to shoulders on these bands. Eigenmodes for these eight highest frequency modes are dominated by T-O and O-T-O displacements (Table 2b). Modes at 1160 and 1142 cm^{-1} are dominated by Si-O and O-Si-O motions.

Between 600 and 800 cm^{-1}, the eigenmodes are less localized and include Na motion. Four calculated modes correspond to a cluster of four observed modes between 720 and 790 cm^{-1}. Similar to the Raman-active modes at these frequencies, the eigenmodes at 792 and 749 cm^{-1} feature Si-O-Si deformations coordinated with neighboring Na-O stretch motions (Table 2b). Other calculated modes in this frequency range are dominated by tetrahedral and Na-environment deformations.

Below 600 cm^{-1}, atomic displacements are coordinated among larger atom groups that include four-membered tetrahedral rings and larger tetrahedral cage units, as well as the Na environment. Above 400 cm^{-1}, the displacements are more localized on the four-membered tetrahedral rings, while modes below 400 cm^{-1}, include tetrahedral cage shear and compression-expansion motions.

The valence potential force constant model used for albite by von Stengel (1977) is different from the room-temperature model described above. Most bond-stretch force constant values are significantly different between the two studies. The Si-O stretch force constant value reported here is 4.83×10^{-5} dyne/cm, compared with the 3.9×10^{-5} dyne/cm determined by von Stengel (1977); this is an important difference considering that this force constant describes a large fraction of all bonds in the crystal structure. This difference is probably caused, in part, by a coupling force constant used by von Stengel (1977) that was configured between two T-O bonds with a common oxygen atom. The T-O coupling force constant is a short-coming of the von Stengel (1977) model, because the negative value (-0.8×10^{-5} dyne/cm) is nonphysical. Von Stengel (1977) indicates that for sanidine and microcline, the influence of the negative T-O coupling force constant values creates negative contributions to the potential energy for many eigenmodes generated by the calculations; in a physically meaningful model, atomic displacements should increase, not decrease, the potential energy (Bell, private communication). By coincidence, the Al-O stretch force constant values are nearly identical in both studies. The Na-O stretch force constant values reported in Table 1 are different from the 0.18 Na-O stretch value reported by von Stengel (1977). This difference is due to the manner in which the Na environment was modeled by each study. Von Stengel (1977) inversely weighted, with respect to Na-O distance, the Na-O force constant value for each bond; in the present study, two Na-O stretch and one O-Na-O bend force constants describe the Na environment. The O-Si-O and O-Al-O force constant values reported in Table 1 are also different from the 1.34 and 0.95×10^{-11} erg values reported, respectively, by von Stengel (1977). These differences can, again, be attributed to the way each model was constructed. For example, a T-O-T force constant was used by von Stengel (1977), that was not used here, while an O-Na-O force constant was used here, but not by von Stengel (1977).

Crystalline albite heating

The unpolarized Raman spectra of albite undergo gradual changes upon heating from 25 to 1100 °C (Fig. 5). Relative intensities of most Raman modes stay roughly constant through the temperature range investigated. One major exception is the peak envelope between 140 and 210 cm^{-1}, which steadily increases intensity as temperature increases; this trend is probably due to increased thermal population effects (Born and Huang 1954) on the spectrum as the temperature rises. Spectral features also broaden in general, from near 9 cm^{-1} full-width-half-maximum (FWHM) at room temperature to approximately 25 cm^{-1} FWHM at 1100 °C. As a result, observed frequencies assigned to specific modes at higher temperatures are more uncertain than frequency assignments made for the 25 °C data. Some features disappear under broadening shoulders of prominent neighboring peaks, such as the room temperature mode at 578 cm^{-1}. Frequencies steadily decrease by 15 to 27 cm^{-1} for modes between 600 to 1200 cm^{-1}, as the temperature increases from 25 to 1100 °C. These higher-frequency modes are due to more localized atomic displacements. Frequency vs. temperature behavior is more complicated for modes below 600 cm^{-1}, where the frequency shifts are small. For some features, such as the 25 °C modes at 289, 327, and 505 cm^{-1}, no shifting takes place.

The triclinic to monoclinic transition near 980 °C does not have a dramatic effect on the unpolarized spectrum (Fig. 5). This is probably due to the thermal broadening of the Raman features dominating any effects that would be caused by the structural rearrangements (i.e., Al and Si disorder as well as changes in the tetrahedral cage configuration around Na). The rate of change of mode frequency vs. temperature is roughly linear throughout the temperature range covered. Noticeable changes in the number of modes would not be expected in the unpolarized data, since the phase transition splits the 39 Raman-active A_g modes for triclinic

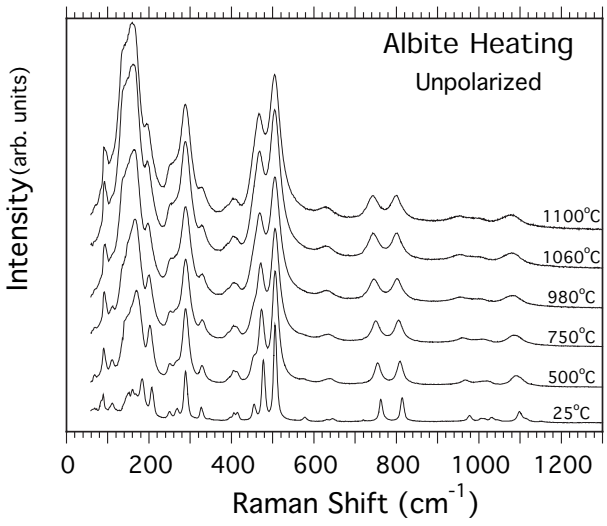

FIGURE 5. Unpolarized Raman spectra of crystalline albite from room temperature to 1100 °C.

albite into 20 A_g and 19 B_g modes for monoclinic albite.

The steady decrease of mode frequencies between 550 to 1200 cm^{-1} as the temperature rises (Fig. 5) affects the resulting T-O and Na-O stretch force constants determined from the LD fittings (Tables 1 and 4). Average T-O stretch force constants decrease by less than 5% as the temperature increases. The Na-O(long) bond stretch values decrease the most, by approximately 25%, from 25 to 1060 °C. The findings by Winter et al. (1979) indicate that the geometry of the individual tetrahedra do not change much with respect to temperature, but atomic thermal vibration parameters increase significantly, which can explain the Raman peak broadening, and possibly, the mode frequency shifts. O-T-O bond bending force constant values do not vary much with respect to temperature.

The final rms value for each fit is larger and less meaningful at higher temperatures due to the greater uncertainty of the frequency determination for each observed mode. Several calculated modes have frequencies that are under broad spectral features, and the specific observed frequencies assigned to these modes cannot be clearly determined. Therefore, more undetermined observed mode frequencies are present for the 1060 °C calculation (Tables 5a and b) than for the 25 °C calculation (Tables 2a).

1060 °C albite: A_g and B_g spectra—lattice dynamics results

Polarized Raman spectra were collected for monoclinic albite at 1060 °C in an attempt to segregate the A_g modes from the B_g modes (Figs. 6a and 6b). Peaks in these spectra are broadened to the point where they combine with neighboring features to form peak envelopes over frequency ranges. Only 27 observed Raman-active mode frequencies were used as targets for the 39 calculated A_g and B_g modes. The calculations place groups of modes within the frequency ranges of these envelopes so that it is difficult to discern which calculated mode corresponds to which peak in certain frequency intervals. As a result, generalized atomic displacements were assigned to each peak envelope. Eigenmodes assigned to spectral features within the various frequency ranges for 1060 °C albite (Figs. 6a and b; and Tables 5a and 5b) basically correspond with eigenmodes determined for equivalent spectral features at 25 °C (Fig. 2 and Table 2a).

Above 900 cm^{-1}, LD indicated eight A_g modes for triclinic albite split into three A_g modes and five B_g modes for monoclinic albite. The enhanced amplitude of the 1008 cm^{-1} mode in the B_g spectrum is accounted for by LD, which calculates a 1020 cm^{-1} B_g mode. Therefore the 1008 cm^{-1} feature was assigned to the B_g species. Other peaks above 900 cm^{-1} can be assigned to both A_g and B_g species modes, where the corresponding eigenmodes are dominated by T-O stretch and O-T-O bend motions.

Between 900 and 550 cm^{-1}, seven A_g modes for triclinic albite split into four A_g and three B_g modes for monoclinic albite. The 800 and 745 cm^{-1} peaks are more prominent with regard to the surrounding spectral features in the A_g spectrum. LD assigned three A_g modes and one B_g mode to these two peaks. The calculations placed the B_g mode at 748 cm^{-1}, so that the 745 cm^{-1} peak was assigned to the B_g species (Fig. 6b). The 632 cm^{-1} peak present in both spectra corresponds to the calculations placing an A_g and a B_g mode near this frequency. Another B_g mode was placed by the calculations under the high-frequency shoulder of the large 505 cm^{-1} peak, where no specific observed frequency could be assigned (similar to the 25 °C spectrum). The two prominent peaks at 800 and 745 cm^{-1} were assigned to T-O-T breathing and neighboring Na-O stretches.

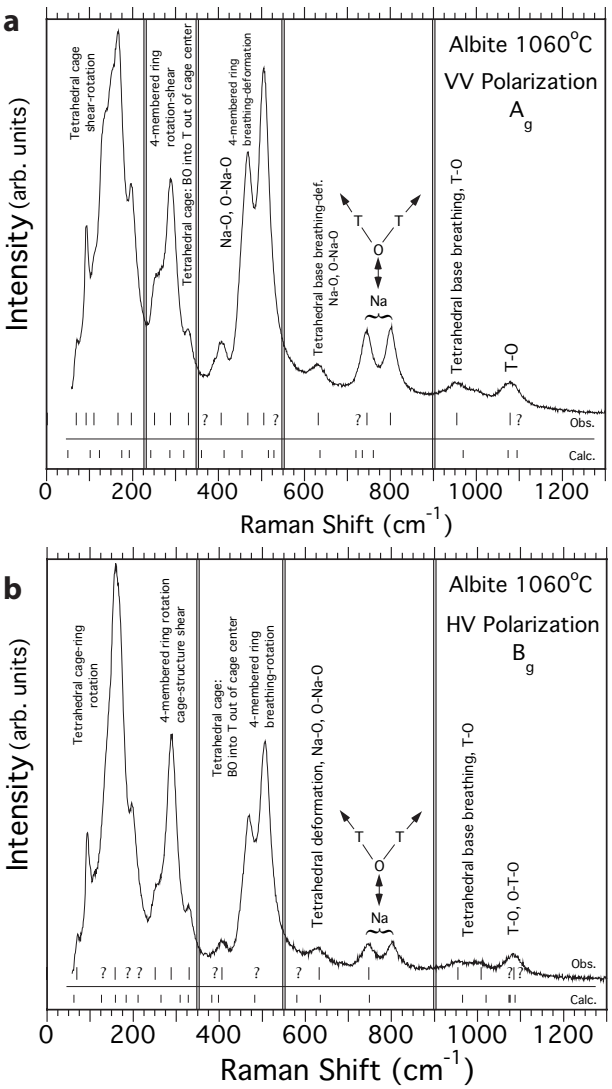

FIGURE 6. Polarized Raman spectra of albite at 1060 °C, indicating vibrational assignments for the A_g species modes (parallel polarized) in (**a**), and for the B_g species modes (cross polarized) in (**b**).

Between 550 and 350 cm^{-1}, eight A_g modes for triclinic albite split into five A_g and three B_g modes for monoclinic albite. The corresponding spectral features are more prominent in the A_g spectrum. LD assigned A_g modes to all peaks within this frequency range. One B_g mode was assigned to the two prominent peaks at 505 and 468 cm^{-1}, where an observed frequency assignment cannot be clearly determined. The 406 cm^{-1} peak was assigned to an A_g mode and a B_g mode by the calculations. Eigenmodes within this frequency range are dominated by four-membered ring rotation-breathing and Na motions.

Below 350 cm^{-1}, seventeen A_g modes for triclinic albite split into nine A_g modes and eight B_g modes for monoclinic albite. The 330, 288, and 251 cm^{-1} peak cluster appears to be more prominent

in the B_g spectrum, but the calculation assigned three modes each for the A_g and B_g species within this frequency interval. The prominent peak cluster near 160 cm^{-1} shows complicated polarization dependence, where LD assigned five modes each to the A_g and B_g species. Eigenmodes for these lowest frequency features are dominated by four-membered ring and tetrahedral cage shear-rotation displacements.

Albite melting

As the albite crystal is heated above 1118 °C, Raman amplitudes in the unpolarized spectra gradually decrease (Fig. 7), while black-body radiation becomes more noticeable at the higher frequencies. Higher frequency Raman features become difficult to distinguish from the black body contributions, especially for the 1320 °C crystal and melt spectrum. At 550 cm^{-1} and lower, the broadened Raman peaks gradually transformed to the low-frequency envelope for albite melt. Melting was sluggish, where crystal and melt appear to coexist for the 1200, 1245, and 1270 °C spectra, and the volume of the crystalline component decreases with increasing temperature. The melt contribution became most apparent at 1320 °C, when after several minutes the sample completely melted (Fig. 7, top). This behavior was reproduced by heating another albite fragment to the same temperatures in a calibrated Deltech furnace, where the sample was removed from the furnace for direct observation at each temperature of interest.

Albite melt-glass cooling

The albite melt was cooled in stages from 1320 °C, where the sample remained amorphous to room temperature (Fig. 8). It was not possible to determine from the spectra the temperature at which melt transformed to glass. Albite glass spectra were measured at 1075, 540, and 25 °C, where the VV Raman spectrum for room temperature albite glass is similar to that reported in McKeown et al. (1984). As the sample cooled, the spectra changed in two ways: (1) the 100 cm^{-1} band lost intensity, and (2) frequency shifts took place, especially for bands above 700 cm^{-1}. The 100 cm^{-1} band is probably due to thermal population effects (Born and Huang 1954) in the glass and would naturally decrease in amplitude when the sample is cooled. Highest frequency bands near 940 and 1070 cm^{-1} shift to higher frequency by approximately 40 cm^{-1}. Bands below 900 cm^{-1} change shape as well as increase in frequency by approximately 15 to 25 cm^{-1}; this is basically the reverse of those trends observed for the albite crystal upon heating.

Raman spectra for albite melt and glass upon cooling were also presented by Daniel et al. (1995), where the spectral changes at frequencies between 600 and 900 cm^{-1} were mainly attributed to increasing second order Raman effects with increasing temperature. After correcting for these effects, the frequencies and relative intensities of bands above 700 cm^{-1} remained relatively unchanged.

Albite crystal—glass comparison

By comparing the Raman spectra and associated vibrational assignments of crystalline albite at 1060 °C with the spectra of albite melt or glass at similar temperatures, vibrational assignments to some of the spectral features for the crystal may be applied to corresponding spectral bands for the glass or melt. Comparing high-temperature spectra has disadvantages, however, due to peak broadening and poorer signal-to-noise levels. To avoid these short-comings, comparing the room-temperature spectra of crystalline albite with albite glass can be done, while similar vibrational assignments can be made.

In the study of molten silicates, it is assumed that the room-temperature glass can model the melt. The Raman spectra of albite glass and melt generally support this assumption (Fig. 8 and Daniel et al. 1995), where the 25 °C glass spectrum can be used to model the glass near the melting temperature. Similar arguments can be made for the Raman spectra of crystalline albite as well as the associated eigenmodes, because the vibrational assignments generally track with the spectral features from 25 to 1060 °C (Figs. 2 and 6). In the case of crystalline albite, a disordered T-site room temperature structure can be used to ap-

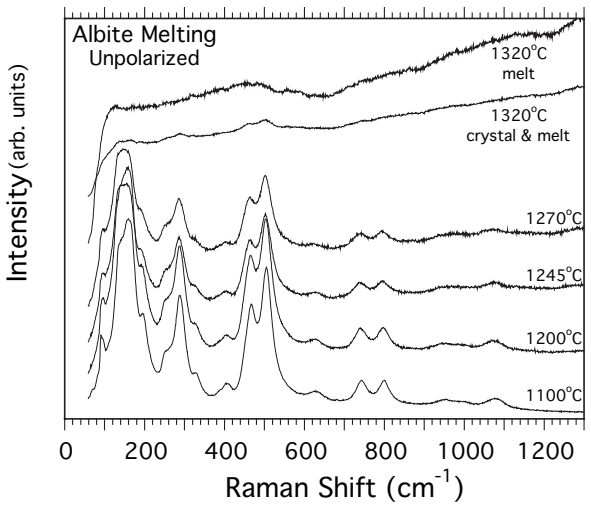

FIGURE 7. Unpolarized Raman spectra of albite from the crystalline state at 1100 °C to completely melted at 1320 °C.

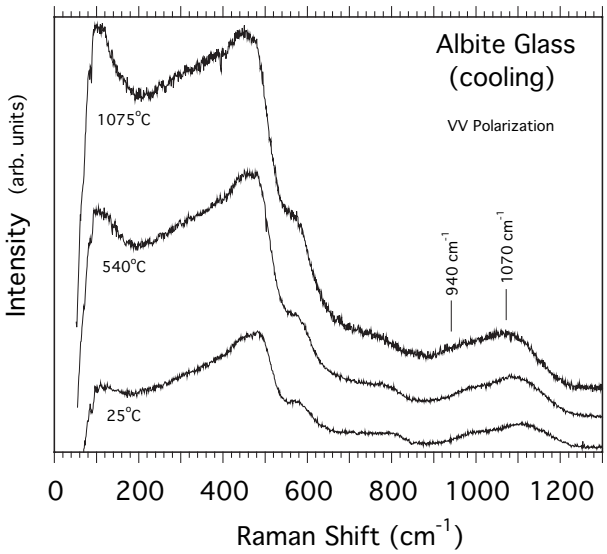

FIGURE 8. Parallel polarized Raman spectra of the albite glass cooling to room temperature.

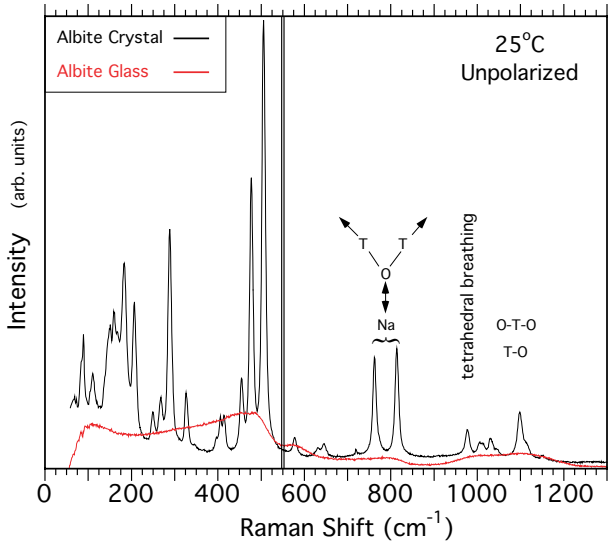

FIGURE 9. Comparison of the room temperature unpolarized spectra of crystalline albite (before melting) and albite glass (after melting). Some of the higher-frequency vibrational mode assignments are shown.

proximate the high temperature structure.

Comparing the 25 °C unpolarized spectrum of albite glass to the crystal can be done by dividing the spectra into two frequency ranges (Fig. 9). Spectral similarities can be observed for the crystal and glass data at frequencies above 550 cm^{-1}. These features are caused by localized atomic displacements that may not be that different between crystal and glass, as supported by earlier arguments (McKeown et al. 1984, 1985) that indicate similar local Al and Si environments in albite crystal and glass. Few similarities are seen between the crystal and glass spectra below 550 cm^{-1}. These modes are generally caused by atomic displacements coordinated over larger atom clusters that include tetrahedra and Na atoms. The differences between the crystalline albite and albite glass Raman spectra can be further explained by the findings of Taylor and Brown (1979), where the four-membered tetrahedral ring-based structure in crystalline albite changes to a six-membered tetrahedral ring-based network structure upon melting. This change indicates that the local structures within crystal and melt are similar, but environments including larger atom clusters change significantly, such as bond angles between tetrahedra.

Above 550 cm^{-1}, sets of peaks for albite crystal can be correlated to broad bands for albite glass. Crystalline albite modes at 1170, 1151, 1116, and 1098 cm^{-1} correspond to the band near 1120 cm^{-1} for albite glass; crystalline albite modes at 1046, 1030, 1005, and 977 cm^{-1} correspond to the band near 1010 cm^{-1} for albite glass (McKeown et al. 1984). A_g modes within this frequency range are assigned to T-O and O-T-O displacements, which generally agree with the Si-O and T-O(bridging) assignments made earlier for the glass bands near 1120 and 1010 cm^{-1} (McKeown et al. 1984). Between 550 and 900 cm^{-1}, two prominent crystalline albite peaks at 814 and 762 cm^{-1} correspond to the albite glass band near 800 cm^{-1}. The crystalline albite peaks are assigned to T-O-T breathing and neighboring Na-O stretch motions (Fig. 9). This assignment may apply to the albite glass band near 800 cm^{-1} and is new information, considering that an older assignment for this band does not involve Na (McKeown et al. 1984). One other set of crystal-glass features can be compared and includes the 578 cm^{-1} peak for crystalline albite and the albite glass band near 590 cm^{-1}. The crystalline albite 578 cm^{-1} peak was assigned to tetrahedral as well as Na environment deformations, which may apply to the albite glass band near 590 cm^{-1}.

Below 550 cm^{-1}, the only spectral features to compare are the most intense crystal modes at 505 and 477 cm^{-1}, with the broad albite glass envelope and its peak near 485 cm^{-1}. LD show that the crystalline modes are dominated by four-membered tetrahedral ring and Na environment compression-expansion motions. T-O-T bending and bridging-oxygen breathing modes within tetrahedral rings, have been assigned to Raman features near 485 cm^{-1} for albite glass and other silicate glasses, where larger ring sizes correlate to lower the mode frequencies (Galeener 1982; Matson et al. 1986; McKeown et al. 1984). The albite glass spectral features near 500 cm^{-1} are generally shifted to lower frequencies compared with their crystalline counterparts (Fig. 9), which indicates that the average ring size is larger for the glass compared with the crystal, and is consistent with the findings of Taylor and Brown (1979).

ACKNOWLEDGMENTS

I thank J. Post and P. Pohwat (Mineral Sciences Department, Smithsonian Institution) for providing the albite crystals, as well as C. Mooers (Vitreous State Laboratory, VSL) for performing the SEM-EDS analyses. I also thank W. Lutze (VSL) for translating von Stengel (1977).

REFERENCES CITED

Atkinson, A.J., Carpenter, M.A., and Salje, E.K.H. (1999) Hard mode infrared spectroscopy of plagioclase feldspars. European Journal of Mineralogy, 11, 7–21.

Born, M. and Huang, K. (1954) Dynamical Theory of Crystal Lattices, p. 199. Clarendon Press, Oxford.

Brawer, S.A. and White W.B. (1975) Raman spectroscopic investigation of the structure of silicate glasses (I). The binary alkali silicates. Journal of Chemical Physics, 63, 2421–2431.

Couty, R. and Velde, B. (1986) Pressure-induced band splitting in infrared spectra of sanidine and albite. American Mineralogist, 71, 99–104.

Daniel, I., Gillet, Ph., Poe, B.T., and McMillan, P.F. (1995) In-situ high temperature Raman spectroscopic studies of aliminosilicate liquids. Physics and Chemistry of Minerals, 22, 74–86.

Dowty, E. (1987a) Fully automated microcomputer calculation of vibrational spectra. Physics and Chemistry of Minerals, 14, 67–79.

——— (1987b) Vibrational interactions of tetrahedra in silicate glasses and crystals. Physics and Chemistry of Minerals, 14, 122–138.

Fateley, W.G., Dollish, F.R., McDevitt, N.T., and Bentley, F.F. (1972) Infrared and Raman Selection Rules for Molecular and Lattice Vibrations: the Correlation Method. Wiley, New York.

Freeman, J.J., Wang, A., Kuebler, K.E., and Haskin, L.A., (2003) Raman spectroscopic characterization of the feldspars—implications for in situ surface mineral characterization in planetary exploration. Lunar and Planetary Science, XXXIV, 1676.

Galeener, F.L. (1982) Planar rings in vitreous silica. Journal of Non-Crystalline Solids, 49, 53–62.

Goncharov, A.F. and Struzhkin, V.V. (2003) Raman spectroscopy of metals, high-temperature superconductors, and related materials under high pressure. Journal of Raman Spectroscopy, 34, 538–548.

Kim, C.C., Bell, M.I., and McKeown, D.A. (1993) Vibrational Analysis of benitoite and the Si_3O_9 ring. Physical Review B, 47, 7869–7877.

Kracek, F.C., Neuvonen, K.J., and Burley, G. (1951) Thermochemistry of mineral substances, I: A thermodynamic study of the stability of jadeite. Journal of the Washington Academy of Sciences, 41, 377.

Matson, D.W., Sharma, S.K., and Philpotts, J.A. (1986) Raman spectra of some tectosilicates and of glasses along the orthoclase-anorthite and nepheline-anorthite joins. American Mineralogist, 71, 694–704.

McKeown, D.A., Galeener, F.L., and Brown, G.E., Jr. (1984) Raman studies of Al coordination in silica-rich sodium aluminosilicate glasses and some related minerals. Journal of Non-Crystalline Solids, 68, 361–378.

McKeown, D.A., Waychunas, G.A., and Brown, G.E., Jr. (1985) EXAFS study of the aluminum coordination environment in a series of silica-rich glasses and selected minerals within the sodium aluminosilicate system. Journal of Non-Crystalline Solids, 74, 349–371.

McKeown, D.A., Bell, M.I., and Kim, C.C. (1993) Raman spectroscopy of silicate rings: benitoite and the 3-membered ring. Physical Review B, 48, 16357–16365.

McKeown, D.A., Bell, M.I., and Etz, E.S. (1999a) Vibrational analysis of the trioctahedral mica phlogopite. American Mineralogist, 84, 970–976.

——— (1999b) Vibrational analysis of muscovite: a dioctahedral mica. American Mineralogist, 84, 1041–1048.

McMillan, P., Piriou, B., and Navrotsky, A. (1982) A Raman spectroscopic study of glasses along the joins silica-calcium aluminate, silica-sodium aluminate, and silica-potassium aluminate. Geochimica et Cosmochimica Acta, 46, 2021–2037.

Mysen, B.O., Virgo, D., and Scarfe, C.M. (1980) Relations between the anoinic structure and viscosity of silicate melts—A Raman spectroscopic study. American Mineralogist, 65, 690–710.

Ribbe, P., Ed. (1975) Feldspar Mineralogy, 2nd ed., 30–40. Reviews in Mineralogy, The Mineralogical Society of American, Chantilly, VA.

Rossman, G.R. (2004) Mineral Spectroscopy Server: http://minerals.gps.caltech.edu/.

Smith, J.V. (1974) Feldspar Minerals I. Crystal Structure and Physical Properties. Springer-Verlag, Heidelberg.

Taylor, M. and Brown, G.E., Jr. (1979) Structure of mineral glasses—I. The feldspar glasses $NaAlSi_3O_8$, $KAlSi_3O_8$, $CaAl_2Si_2O_8$. Geochimica et Cosmochimica Acta, 43, 61–75.

Taylor, M., Brown, G.E., Jr., and Fenn, P.M. (1980) Structure of mineral glasses—III. $NaAlSi_3O_8$ supercooled liquid at 805 °C and the effects of thermal history. Geochimica et Cosmochimica Acta, 44, 109–117.

von Stengel, M.O. (1977) Normalschwingungen von alkalifeldspaten. Zeitschrift fur Kristallographie, 146, 1–18.

White, W.B. (1975) Structural interpretation of lunar and terrestrial minerals by Raman spectroscopy. In C. Karr, Ed., Infrared and Raman spectroscopy of lunar and terrestrial materials, p. 343. Academic Press, New York.

Winter, J.K., Okamura, F.P., and Ghose, S. (1979) A high-temperature structural study of high albite, monalbite, and the analbite to monalbite phase transition. American Mineralogist, 64, 409–423.

MANUSCRIPT RECEIVED MAY 26, 2004
MANUSCRIPT ACCEPTED FEBRUARY 11, 2005
MANUSCRIPT HANDLED BY BRIGITTE WOPENKA